Elsevier Editorial System(tm) for Journal Of Computational Physics
Manuscript Draft

Manuscript Number:

Title: Discontinuous Finite Element Solution of the Radiation Diffusion Equation on Arbitrary Polygonal Meshes and Locally Adapted Quadrilateral Grids

Article Type: Regular Article

Keywords: Radiation Diffusion; Arbitrary Polygonal Grids; Discontinuous Finite Element; Adaptive Mesh Refinement

Corresponding Author: Dr. Jean C Ragusa, PhD

Corresponding Author's Institution: Texas A&M University

First Author: Jean C Ragusa, PhD

Order of Authors: Jean C Ragusa, PhD

Abstract: In this paper, we propose a piece-wise linear discontinuous (PWLD) finite element discretization of the diffusion equation for arbitrary polygonal meshes. It is based on the standard diffusion form and uses the symmetric interior penalty technique, which yields a symmetric positive definite linear system matrix. A preconditioned conjugate gradient algorithm is employed to solve the linear system.
Piece-wise linear approximations also allow a straightforward implementation of local mesh adaptation by allowing unrefined cells to be interpreted as polygons with an increased number of vertices.
Several test cases, taken from the literature on the discretization of the radiation diffusion, are presented: random, sinusoidal, Shestakov, and Z meshes are used. The last numerical example demonstrates the application of the PWLD discretization to adaptive mesh refinement.

Suggested Reviewers: Todd Palmer PhD
Professor, Nuclear engineering, Oragon State University
palmerts@engr.orst.edu
expert in radiation transport;

has worked on the discretization of the diffusion equation on polygonal meshes (references 2 and 9 cited in our manuscript)

Teresa Bailey PhD
research scientist, LLNL
bailey42@llnl.gov
has developed a piece-wise linear continuous FEM solution technique of the diffusion equation for polygonal/polyhedral grids (published in JCP in 2008)

has worked on the discretization of the diffusion equation on polygonal meshes (references 6, 7, and 21 cited in our manuscript)

expert in radiation transport;

Jim Morel PhD
Professor, Nuclear engineering, Texas A&M university
morel@tamu.edu
expert in radiation transport;

has worked on the discretization of the diffusion equation on polygonal meshes, developing the mimetic finite difference technique (references 10, 11, 12, 17, 18, and 33 cited in our manuscript)

Mikhail Shashkov PhD
research scientist, XCP-4 Methods and Algorithms, LANL
shashkov@lanl.gov
expert in radiation transport;

has worked on the discretization of the diffusion equation on polygonal meshes, developing the mimetic finite difference technique (references 3, 5, 8, 10, 11, 12 and 38 cited in our manuscript)

Jean Ragusa
Department of Nuclear Engineering
Texas A&M University
College Station, TX 77843-3133, USA
phone: (979) 862 2033
e-mail: jean.ragusa@tamu.edu

August 13, 2013

Professor William Martin
Editor,
Journal of Computational Physics

Dear Professor Martin,

Please find attached a copy of our manuscript titled "Discontinuous Finite Element Solution of the Radiation Diffusion Equation on Arbitrary Polygonal Meshes and Locally Adapted Quadrilateral Grids" for submission to the *Journal of Computational Physics*.

In this paper, we propose a piecewise linear *discontinuous* finite element discretization of the standard diffusion equation for arbitrary polygonal grids.

This work follows closely prior works by Jim Morel (LANL, now TAMU), Mikhail Shashkov (LANL), Teresa Bailey (LLNL), Marvin Adams (TAMU), and Todd Palmer (OSU).

Our work is based on the standard diffusion form and uses the symmetric interior penalty technique, which yields a symmetric positive definite linear system matrix. A preconditioned conjugate gradient algorithm is employed to solve the linear system. Piecewise linear approximations also allow a straightforward implementation of local mesh adaptation by allowing unrefined cells to be interpreted as polygons with an increased number of vertices. Several test cases, taken from the literature on discretizations of the radiation diffusion, are presented: random, sinusoidal, Shestakov, and Z meshes are used. The last numerical example demonstrates the application of the PWLD discretization to adaptive mesh refinement.

Employing a DFEM approximation to solve the diffusion equation is not commonly done (especially on polygonal grids), but this will allow us to use proven DFEM-based DSA preconditioners to tackle radiation transport problems on polygonal grids in the future.

Thank you for considering this manuscript for publication in JCP.

Best regards,

Jean Ragusa

Discontinuous Finite Element Solution of the Radiation Diffusion Equation on Arbitrary Polygonal Meshes and Locally Adapted Quadrilateral Grids

Jean C. Ragusa

Department of Nuclear Engineering, Texas A&M University, College Station, TX 77843, USA

Abstract

In this paper, we propose a piece-wise linear discontinuous (PWLD) finite element discretization of the diffusion equation for arbitrary polygonal meshes. It is based on the standard diffusion form and uses the symmetric interior penalty technique, which yields a symmetric positive definite linear system matrix. A preconditioned conjugate gradient algorithm is employed to solve the linear system. Piece-wise linear approximations also allow a straightforward implementation of local mesh adaptation by allowing unrefined cells to be interpreted as polygons with an increased number of vertices. Several test cases, taken from the literature on the discretization of the radiation diffusion, are presented: random, sinusoidal, Shestakov, and Z meshes are used. The last numerical example demonstrates the application of the PWLD discretization to adaptive mesh refinement.

Key words: Radiation Diffusion, Arbitrary Polygonal Grids, Discontinuous Finite Element, Adaptive Mesh Refinement

1. Introduction

This paper deals with a Piece-Wise Linear Discontinuous (PWLD) finite element spatial discretization of the radiation diffusion equation on arbitrary polygonal grids, with and without adaptive mesh refinement. Radiation diffusion is an asymptotic limit of the radiation transport equation and can be written in the following form:

$$-\vec{\nabla}\cdot D(\vec{r})\vec{\nabla}E(\vec{r}) + \sigma_a(\vec{r})E(\vec{r}) = Q(\vec{r}), \tag{1}$$

where E is the radiation energy intensity, D is a diffusion coefficient, σ_a is an opacity coefficient, and Q is the source.

Email address: jean.ragusa@tamu.edu (Jean C. Ragusa)

Several spatial discretizations have been proposed to solve Eq. (1) on arbitrary polygons (2D) and polyhedra (3D) [1, 2, 3, 4, 5, 6, 7, 8]. We review them below. Wachspress [1] developed a family of rational polynomial functions that can be employed as basis functions in a finite element method on polygonal/polyhedral grids. This yields symmetric positive-definite (SPD) matrices but (i) the finite element integrals must be carried out numerically and (ii) the Jacobian of the transformation becomes zero on degenerate cells (such as the ones shown on Fig. 1) and on non-convex cells. Palmer [2, 9] proposed a node-based finite volume method that enforces particle balance over the control volume associated with a given grid vertex. This control volume defines a dual cell constructed as the union of all corners surrounding the specified vertex v. In 2D, a corner is a quadrilateral with the following vertices: vertex p, the cell center, and the midpoint of the edges that contain vertex p. On a triangular grid, Palmer's scheme is equivalent to employing linear continuous finite elements with "mass-matrix lumping". This method is second-order accurate but its discretization of the diffusion equation produces an asymmetric (i.e., not SPD) matrix, in general. Mimetic finite difference methods create discrete analog of vector and tensor calculus in order to accurately approximate the original differential operators; see, e.g., [10]. Mimetic methods preserve important properties of the differential operators such as symmetry, positivity, monotonicity, asymptotic limits, and identities pertaining to tensor and vector calculus. Mimetic methods can also be viewed as mixed hybrid finite element formulations with specific spatial quadratures. In addition to quadrilateral and hexahedral meshes (see, e.g., [11, 12], mimetic finite difference methods have recently been applied to the diffusion equation on arbitrary polygonal grids [3, 4, 5, 8]. Bailey et al. [7] recently employed piece-wise linear basis functions to solve a diffusion equation using a Galerkin finite element technique on arbitrary polygonal and polyhedral grids. Their goal was to devise a *continuous* finite element discretization that does not necessitate numerical integration, yields an SPD matrix, is second-order accurate, and handles arbitrary polygonal/polyhedral grids (including grids with degenerate cells). The approach they followed is a standard Galerkin weak formulation for continuous finite elements, with piece-wise linear basis functions defined on subcells (which they called "sides") of arbitrary polygons/polyhedrons.

In this paper, we are interested in solving a diffusion equation on arbitrary polygonal grids using a *discontinuous* finite element discretization. We employ the Symmetric Interior Penalty (SIP) technique [13, 14, 15], developed for the discretization of elliptic equations using discontinuous Galerkin techniques; this results in a linear system matrix that is Symmetric Positive Definite (SPD). For basis functions, we use the piece-wise linear functions of [7]. The motivations for employing discontinuous finite elements on polygonal grids are as follows:

1. prior works dealing with the spatial discretization of the radiation diffusion equation on polygonal meshes have used finite volume, mimetic finite differences, and continuous finite element techniques; we wish to test the performance of Piece-Wise linear discontinuous finite elements for such

grids;

2. prior works also dealt with spatial discretization errors on highly distorted quadrilateral grids; we wish to assess the accuracy of a PWLD discretization on such grids as well;
3. a diffusion solve often serves as a synthetic accelerator or preconditioner for iterative solution techniques applied to radiation transport problems [16, 17]. On unstructured and polygonal/polyhedral grids, a discontinuous finite element technique is often employed to discretize the transport equation [18, 19, 20, 21, 22]; it was found in [23] that employing the same discretization technique for both the radiation transport solve and its diffusion preconditioner was effective on triangular grids. In developing a PWLD-based diffusion preconditioner for transport solves, one needs to evaluate the effectiveness of a PWLD discretization of the diffusion equation first.
4. It has been proposed that PWL continuous discretizations can more seamlessly handle locally refined grids as produced by Adaptive Mesh Refinement (AMR) algorithms [7]. In [7], the authors generated a grid with two refinement levels and for a problem with a linear solution. Here, we fully embed a PWL discontinuous discretization in an AMR process and test it with more complex solutions.

The remainder of the paper is as follows. In Section 2, we further discuss the use of polygonal meshes, define the piece-wise linear discontinuous basis functions for arbitrary polygons, and examine how polygonal grids can be utilized in handling local mesh refinement (as in AMR approaches). The Symmetric Interior Penalty technique applied to the diffusion equation is reviewed in Section 3. Mesh adaptivity utilizing piece-wise linear basis function is presented in Section 4. Results are provided in Section 5; all of the test cases presented here are borrowed from the literature on spatial discretization techniques applied to the diffusion equation solved on highly distorted quadrilateral grids and polygonal grids.

2. Polygonal Grids and Piece-wise Linear Basis Functions

2.1. Polygonal Meshes and their Application to Adaptive Mesh Refinement

Polygonal cells are an alternative to standard (triangles/quads) mesh partitioning. Mesh generation using polygons (polyhedra in 3D) is an active area of research. Some meshing tools, such as MSTK [24] and the Computational Geometry Algorithms Library [25, 26], may be employed to generate/process polygonal meshes. Several CFD codes (Fluent, StarCCM, OpenFoam) also offer polygonal meshing and solver capabilities. The rationale for polygonal/polyhedral cells is as follows. While quadrilaterals (hexahedra in 3D) can be seen as the standard cell shapes for logically structured meshes, they may be difficult to employ in complex geometries. For unstructured meshes, triangles (tetrahedra in 3D) are the typical building blocks and are employed in numerous automated meshing algorithms, but are not well-suited for boundary layers, for instance, and may require higher cell counts than quad/hex meshes for a similar resolution. The following features of polygonal cells are noteworthy:

- They can provide a better partition of the domain, minimizing the boundary/interior ratio;
- The number of unknowns for an equivalent accuracy/resolution can be reduced (similar to the advantages of hex meshes over tet meshes);
- The notion of transition elements is included by default in arbitrary grids composed of polygons/polyhedra. Therefore, such a grid can easily be split by cut planes, for instance.
- The notion of "hanging nodes" for locally refined/adapted meshed is no longer needed. For example, Fig. 1(a) shows two quadrilateral elements before local refinement; on Fig. 1(b), one of the two cells has been refined. The un-refined cell can now be viewed as a pentagon.

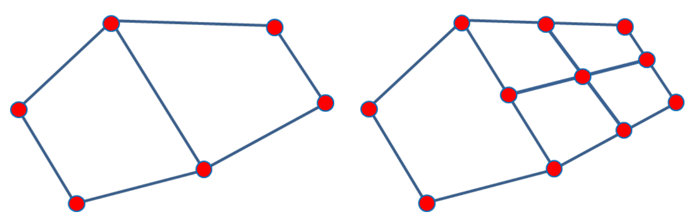

(a) before local refinement (b) after local refinement

Figure 1: Local mesh refinement leads to pentagonal cell

2.2. Piece-wise Linear Basis Functions on Arbitrary Polygons

Here, we describe piece-wise linear finite elements basis functions for arbitrary polygons. Consider a polygonal cell with N_V vertices, (x_i, y_i) for $1 \leq i \leq N_V$. The polygon needs not to be convex. In order to describe the piece-wise linear basis functions for such a cell, we introduce a cell "center", denoted hereafter by $c = (x_c, y_c)$, with $x_c = \sum_{i=1}^{N_V} \alpha_i x_i$ and $y_c = \sum_{i=1}^{N_V} \alpha_i y_i$. We require that $\sum_{i=1}^{N_V} \alpha_i = 1$. Thus, point c can be interpreted as a weighted average of the polygon's vertices. Often, one chooses $\alpha_i = 1/N_V$ but one may also define point c as the centroid of the polygon under consideration. With the introduction of the cell center, the polygon can also be described as N_V triangular subcells (or "sides" if using the terminology of [7]), with each of these triangles being composed of two successive vertices and the cell center. The N_V piece-wise linear basis functions are then given by:

$$b_i(\mathbf{r}) = t_i(\mathbf{r}) + \alpha_i t_c(\mathbf{r}), \qquad i = 1, \ldots, N_V, \tag{2}$$

where $t_i(\mathbf{r})$ is the standard linear function defined on the two adjacent triangular subcells formed by (1) vertex i, vertex $i-1$ and the cell center c, and (2) vertex

i, vertex $i+1$ and the cell center c. t_i is equal to one at the i^{th} vertex and to zero at all other vertices of the polygon, as well as at the cell center. $t_c(\mathbf{r})$ is the "tent" function associated with the cell center and is equal to one at the cell center and to zero at all of the polygon vertices. We stress that this choice of basis functions is not equivalent to employing a standard continuous finite element representation within a polygon Indeed, in the case of a standard continuous finite element representation, the number of basis functions would be equal to $N_V + 1$ (for the N_V vertices and the cell center). In the piece-wise linear representation, the unknowns are only located at the cell vertices and the cell center point is only used to define the basis functions. For example, Fig. 2 presents two simple examples of polygonal cells: a pentagon and a degenerated pentagon, the later is typically obtained during local mesh adaptation (see also Fig. 1(b)). The isolines of the piece-wise linear basis functions for vertex D and E are graphed in Fig. 3 for the regular pentagon and in Fig. 4 for the degenerate pentagon.

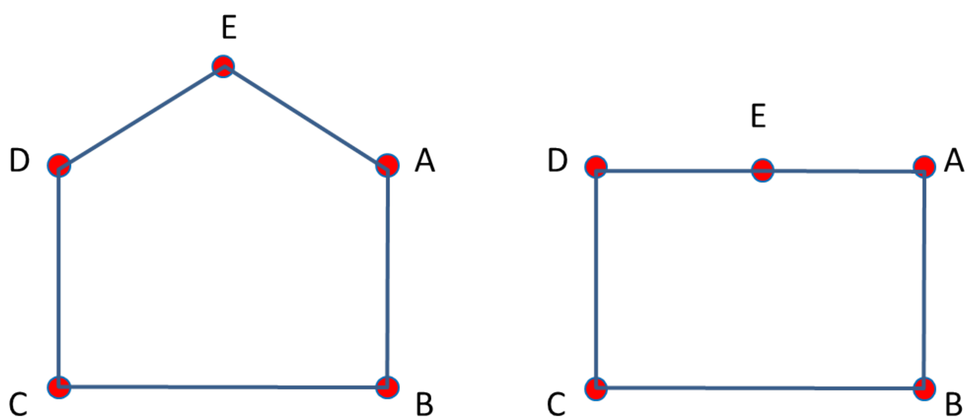

Figure 2: Non-degenerate (left) and degenerate (right) pentagonal cells

3. Discontinuous Finite Element Formulation

In this Section, we present the discontinuous Galerkin finite element technique employed to discretize the radiation diffusion equation on arbitrary polygonal grids. Many variants of such discontinuous discretization methods exist for diffusion problems (depending, for instance, on the choice of stabilization terms, whether the diffusion equation is expressed in its mixed form, ...). We refer the Readers to the review paper [14] for additional details. Here, we employ the Symmetric Interior Penalty (SIP) method which we have found to be robust in our test cases and relatively simple to implement. The general idea of interior penalty methods can be traced back to [27], where the Dirichlet boundary conditions to the model diffusion problem $\{-\vec{\nabla}\cdot\vec{\nabla}E = Q$ in domain $\mathcal{D}$, $E = E^d$ on

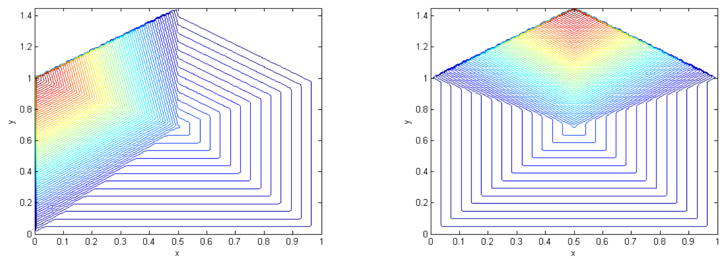

(a) Basis function for Point D

(b) Basis function for Point E

Figure 3: Isolines of PWL basis functions for a non-degenerate pentagon

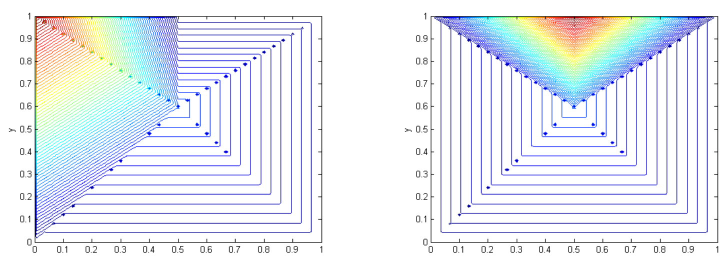

(a) Basis function for Point D

(b) Basis function for Point E

Figure 4: Isolines of PWL basis functions for a degenerate pentagon

the boundary $\partial\mathcal{D}\}$ have been enforced via a penalty method, thereby modifying the boundary condition to read $E+\frac{1}{\mu}\partial_n E = E^d$ with $\mu \gg 1$. Later, Nitsche [28] proposed a consistent formulation for the enforcement of the Dirichlet boundary condition with a penalty term, leading to the weak formulation:

$$\int_{\mathcal{D}} \vec{\nabla}E\cdot\vec{\nabla}b - \int_{\partial\mathcal{D}} \partial_n E b - \int_{\partial\mathcal{D}} \partial_n b E + \int_{\partial\mathcal{D}} \mu(E-E^d)b = \int_{\mathcal{D}} Qb - \int_{\partial\mathcal{D}} E^d \partial_n b, \quad (3)$$

with b a finite element basis function and $\mu = \alpha/h$, where h denotes the mesh size and $\alpha > 1$ is a constant. Nitsche's idea, extended to all cell edges (not only cells with edges on the boundary), leads to the family of interior penalty methods for discontinuous finite elements. The SIP form, which we have chosen here because it is one of the simplest forms and leads to symmetric positive definite matrices, is discussed next. But first, we recall Eq. (1) and specify Dirichlet, Neumann, and Robin boundary condition types on various portions the the domain's boundary: the radiation diffusion equation is given by

$$-\vec{\nabla}\cdot D(\vec{r})\vec{\nabla}E(\vec{r}) + \sigma_a(\vec{r})E(\vec{r}) = Q(\vec{r}) \quad \text{for } \vec{r} \in \mathcal{D}, \quad (4)$$

with Dirichlet boundary conditions

$$E(\vec{r}) = E_0(\vec{r}) \quad \text{for } \vec{r} \in \partial\mathcal{D}^d\,, \quad (5)$$

Neumann boundary conditions

$$-D\partial_n E(\vec{r}) = F_0(\vec{r}) \quad \text{for } \vec{r} \in \partial\mathcal{D}^n, \quad (6)$$

and Robin boundary conditions

$$\frac{1}{4}E(\vec{r}) + \frac{1}{2}D(\vec{r})\partial_n E(\vec{r}) = F^{inc}(\vec{r}) \quad \text{for } \vec{r} \in \partial\mathcal{D}^r\,. \quad (7)$$

E is the unknown radiation scalar intensity. The boundary of the domain is split such that $\partial\mathcal{D} = \partial\mathcal{D}^d \cup \partial\mathcal{D}^n \cup \partial\mathcal{D}^r$, where the superscripts denote Dirichlet, Neumann, and Robin types, respectively. E_0, F_0, and F^{inc} are specified quantities. $\partial_n \boxdot$ denotes $\vec{\nabla} \boxdot \cdot \vec{n}$ with $\vec{n}$ the outward unit normal vector.

3.1. The Symmetric Interior Penalty (SIP) Method

In this paragraph, we describe the SIP discretization [14, 15] applied to the radiation diffusion equation using discontinuous finite elements. We introduce a partition of the domain, $\bigcup_{K\in\mathbb{T}_h} K = \mathcal{D}$, and also assume that the boundary of the domain, $\partial\mathcal{D}$, consists of straight edges only. The set of interior and boundary edges is denoted by $\mathcal{E}_h^i$ and $\mathcal{E}_h^{\partial\mathcal{D}}$, respectively; the set of boundary edges is further split into the three different boundary condition types, i.e.,

$\mathcal{E}_h^{\partial\mathcal{D}} = \mathcal{E}_h^{\partial\mathcal{D}^d} \cup \mathcal{E}_h^{\partial\mathcal{D}^n} \cup \mathcal{E}_h^{\partial\mathcal{D}^r}$. Then, the SIP formulation is given by

$$\begin{aligned}
\int_{\mathbb{T}_h} \Big(D\vec{\nabla} E \cdot \vec{\nabla} b + \sigma_a E b \Big) + \int_{\mathcal{E}_h^i} \Big(\{\!\{ D\partial_n E \}\!\} [\![b]\!] + \{\!\{ D\partial_n b \}\!\} [\![E]\!] + \kappa [\![E]\!] [\![b]\!] \Big) \\
+ \int_{\mathcal{E}_h^{\partial\mathcal{D}^d}} \Big(\kappa E b - D b \partial_n E - D E \partial_n b \Big) + \frac{1}{2} \int_{\mathcal{E}_h^{\partial\mathcal{D}^r}} E b \\
= \int_{\mathbb{T}_h} Q b + \int_{\mathcal{E}_h^{\partial\mathcal{D}^d}} E_0 \Big(\kappa b - D \partial_n b \Big) - \int_{\mathcal{E}_h^{\partial\mathcal{D}^n}} F_0 b + \int_{\mathcal{E}_h^{\partial\mathcal{D}^r}} 2 F^{inc} b \,,
\end{aligned} \tag{8}$$

where we recall that b is a generic test function. In Eq. (8), the last term on the left-hand side and the last two terms on the right-hand side are naturally obtained by applying the Neumman and Robin boundary conditions. The terms pertaining to the Dirichlet boundary conditions are identical to the ones of Nitsche's penalty method. Finally, the interior edge terms are the standard terms due to the extension of Nitsche's method to the interior edges. To generate the linear system associated with Eq. (8), we have opted to use two loops: one over the elements to compute the volume integrals,

$$\int_{\mathbb{T}_h} \longrightarrow \sum_{K \in \mathbb{T}_h} \int_K \,, \tag{9}$$

and one of the edge sets to compute the edge integrals

$$\int_{\mathcal{E}_h} \longrightarrow \sum_{e \in \mathcal{E}_h} \int_e \,. \tag{10}$$

We have also chosen to arbitrarily assign a unit normal vector, $\vec{n}$, to each interior edge (for the boundary edges, $\vec{n}$ is always to outward point unit normal vector). With this choice, the definition of the mean value and the jump of a quantity u on any given interior edge are given by

$$\{\!\{ u \}\!\} = \frac{u^+ + u^-}{2} \tag{11}$$

and

$$[\![u]\!] = u^+ - u^- \,, \tag{12}$$

respectively. The values taken by the quantity u while approaching the edge from either one of its sides are defined as follows:

$$u^{\pm} = \lim_{s \to 0^{\pm}} u(\vec{r} + s\vec{n}) \,, \tag{13}$$

for any point $\vec{r}$ on that edge (that is, u^+ is the trace of u along that edge taken from the cell pointed by $\vec{n}$). The penalty coefficient, κ, is edge-dependent and is given by

$$\kappa_e = \begin{cases} \frac{C}{2} \left(\frac{D^+}{h_\perp^+} + \frac{D^-}{h_\perp^-} \right) & \text{for interior edges, i.e., } e \in \mathcal{E}_h^i, \\ 2C \frac{D^-}{h_\perp^-} & \text{for boundary edges, i.e., } e \in \partial\mathcal{E}_h^{\partial\mathcal{D}} \end{cases} \,, \tag{14}$$

where C is a constant, $h_\perp$ is the length of the cell in the direction orthogonal to edge e. For quadrilateral meshes with linear basis functions, researchers typically utilize $C \geq 4$ (through the formula $C = c(p+1)^2$, with $c \geq 1$ and p the polynomial order). Here, we use $C = 4$. For boundary edges, Kanschat [15] noted that doubling the value of C (on quadrilateral meshes) was beneficial; we have followed their recommendations. In Eq. (14), the $\pm$ superscripts represent again values taken from either side of an edge. For triangular cells, $h_\perp$ is exactly given by $h_\perp = \frac{2A}{L_e}$ where A is the triangle area and L_e is the length of edge e. However, there are no formulae to compute $h_\perp$ for arbitrary polygons. In [29], polygonal cells were assumed to be regular polygonal cells, in which case $h_\perp^{reg}$ is given by twice the inradius for regular even-sided polygons and by the inradius plus the circumradius for odd-sided polygons. The inradius and the circumradius are computed using the area and perimeter of the actual polygonal cell.

4. Adaptive Mesh Refinement Using PWLD Basis Functions

Solutions with strong and rapid spatial variations can be accurately captured using mesh adaptivity [30]. Adaptive Mesh Refinement (AMR) techniques require local error estimates to determine which cells to refine. When using discontinuous finite elements, the numerical solution is discontinuous across the edges (faces in 3D) between neighboring cells. The magnitude of these jumps is small in regions where the solution is smooth and can be significantly larger in regions where the solution undergoes rapid spatial variations. A heuristic local error indicator is, therefore, to monitor the interfacial jumps. Following [31, 22], we define the error indicator on cell K as:

$$\eta_K = \frac{\int_{\partial K} |[\![E]\!]|_{\partial K}}{\text{meas}(\partial K)} \,. \tag{15}$$

The cells flagged for refinement are such that

$$\eta_K \geq \theta \max_{K' \in \mathbb{T}_h} \left(\eta_{K'} \right) \,, \tag{16}$$

where $0 \leq \theta \leq 1$ is a user-specified coefficient. Eq. (16) signifies that cells selected for refinement are such that their error, normalized to the largest error, is larger than or equal to θ.

As noted in the Introduction, piece-wise linear basis functions can be beneficially used to handle transitions between mesh cells of different refinement levels. In the context of discontinuous finite elements, the analog of Fig. 1 is shown in Fig. 5. With standard linear discontinuous finite element representation, the cell that will not undergo refinement (labeled K in Fig. 5(a)) would remain a quadrilateral after refinement of its neighbor, cell K'; with such a representation, the restriction of the intensity along edge AB of cell K would remain a linear function. However, when employing PWLD basis functions, cell K becomes a pentagon after refinement of its neighbor and the restriction of

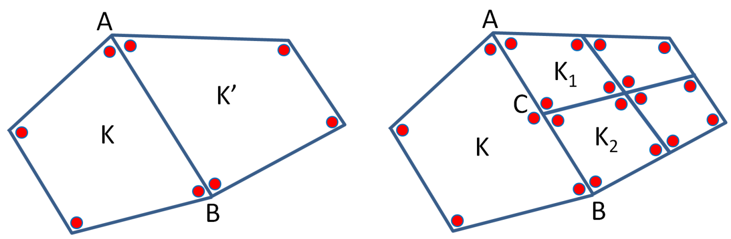

(a) before local refinement (b) after local refinement

Figure 5: Local mesh refinement using piece-wise linear discontinuous basis functions

the intensity along the "degenerate" edge AB of that pentagon now becomes piece-wise linear.

In this work, we only consider the application of piece-wise linear functions to AMR for grids that are initially composed of quadrilateral cells only and refine cells flagged for adaptivity by subdividing them into four children cells; the child cell contains the following four vertices: one of the corners of its parent cell, the midpoint of the two edges that contain that corner, and the centroid of the parent cell. For simplicity in the refinement process, we also limit the refinement level differences between neighboring cells to one, but stress that this is not at all a limitation of PWLD functions. Furthermore, with standard finite element representations, one often imposes refinement of a cell when three or more of its neighbors at the same refinement depth have already been further refined (known as Bank's k-neighbor rule, [32]). Such a situation would arise for a quadrilateral cell when at least three of its four neighbors have been refined, then, according to Bank's rule, that quadrangle would also have to be refined. However, with PWLD functions, such a cell is viewed as a heptagon (three of its neighbors have been refined) with seven unknowns located at the heptagon's vertices or as an octagon (all four neighbors have been refined) with eight unknowns.

5. Numerical Results

Solution techniques that preserve linear solutions, are second-order accurate, and do not suffer excessively from a mesh imprint (especially when using highly distorted grids) have been a topic of research in numerous publications dealing with the discretization of the the radiation diffusion equation . Our numerical examples are taken from that literature. Earlier works focused on quadrilateral (and hexahedral) grids [33, 11, 12, 2] and, therefore, we also provide results obtained using four types of quadrilateral meshes used in those publications:

1. "random" grids, obtained by displacing interior vertices of a uniform orthogonal grid by a fraction of the original cell width: $\pm\xi\delta x$ along the x-axis and $\pm\xi\delta y$ along the y-axis, where $\delta x\,,\delta y$ is the grid resolution and

ξ is a random number ($0 \le \xi \le 1$). $\xi = 0$ returns the original rectangular grid. In the literature, a value of ξ in the order of 0.25 or less is often employed; here we show results with ξ up to 0.65. Above 0.65, some of the original cells are often flipped onto themselves.

2. "'sinusoidal" grids, given by the transformation

$$x_{i,j} = \hat{x}_i + \zeta L_x \sin(2\pi\hat{x}_i/L_x)\sin(2\pi\hat{y}_i/L_y)$$
$$y_{i,j} = \hat{y}_i + \zeta L_y \sin(2\pi\hat{x}_i/L_x)\sin(2\pi\hat{y}_i/L_y)$$

with $(\hat{x}_i, \hat{y}_i)$ the vertices of a uniform orthogonal grid over the rectangular domain $[0\,, L_x] \times [0\,, L_y]$, and ζ a distortion parameter ($0 \le \zeta \le 1/(2\pi)$). A rectangular mesh is recovered when $\zeta = 0$. ζ is user-specified and not randomly generated.

3. Kershaw's "Z-mesh" [34]. For Z-meshes, the skewness parameter s varies between 0 (extremely skewed) and 0.5 (structured rectangular) but note that here, s is user-specified and not randomly generated.
4. "Shestakov" grids (due to Shestakov & Kershaw, [35, 36]). For Shestakov meshes, the randomness parameter a varies between 0 (extremely distorted) and 0.5 (structured rectangular).

The Z- and Shestakov meshes are meant to model grid distortions that occur in Lagrangian hydrodynamic simulations.

Our examples using polygonal grids are also taken from the current literature [3, 4, 7]. The polygonal grids employed here are generated by computing a bounded Voronoi diagram, using the vertices generated from one of the previous quadrilateral meshes (either the random, sinusoidal, Z-mesh, or Shestakov quadrilateral grids). The Voronoi diagram is bounded to the size of the original quadrilateral mesh.

The discrete linear system of equation is solved using a preconditioned conjugate gradient (PCG) algorithm. SSOR and aggregation Algebraic MultiGrid [37] are used as preconditioner. A reduction of the initial residual norm by a factor of 10^{10} is used as the stopping criterion for PCG.

5.1. A Standard Problem with Linear Exact Solution

A standard test problem to verify that a numerical scheme preserves linear solutions has been proposed by Morel et al. [33]. This test consists in solving the radiation diffusion equation on a rectangular domain containing an homogeneous pure scatterer material ($\sigma_a = 0$), no volumetric sources ($Q = 0$), with reflective boundary conditions on the top and bottom faces, and Robin boundary conditions on the left and right faces

$$E(0) - 2D\ \partial_x E|_0 = 4F^{inc}\ \forall y \text{ at } x = 0, \tag{17}$$
$$E(L_x) + 2D\ \partial_x E|_{L_x} = 0\ \forall y \text{ at } x = L_x. \tag{18}$$

The exact solution (for a domain of length L_x in the x-direction) is

$$E(x, y) = \frac{4F^{inc}}{L_x + 4D}\,(L_x + 2D - x) \tag{19}$$

Fig. 6 presents the isolines obtained for this problems using four different quadrilateral grids: (a) a 16×16 random grid obtained by randomly moving the vertices of a rectangular grids by 66% ($\alpha = 0.66$), (b) a 20×20 Z-mesh with a skewness factor of $s = 0.05$ (recall that for Z-meshes, skewness increases as $s \to 0$), (c) a 16×16 Shestakov grid with a randomness factor of $a = 0.15$ (recall also that for Shestakov meshes, randomness increases as $a \to 0$), and (d) a small 3×3 non-convex grid due to Shashkov [38]. Table 1 summarizes the numbers of non-convex quadrilaterals in each of these grids. For instance, the randomized rectangular grid with $\alpha = 0.66$ contains about 21% of non-convex cells. The linearity of the true solution is exactly reproduced by the piece-wise linear discontinuous finite element solution. In the example chosen ($L = 1$,$D = 2$, $F^{inc} = 9$), the solution varies from 20 (left) to 16 (right). Each isoline on the plots represents an increment of 0.2 in the solution.

Fig. 7 presents solutions obtained using polygonal grids; the polygonal grids are based on their quadrilateral equivalents, that is, the vertices of a given type of quadrilateral grids are utilized to generate a bounded Voronoi digram. Hence, we still refer to the polygonal meshes as random mesh, Z-mesh, and Shestakov mesh. For instance, one can note that the polygonal versions of the Z-mesh and the Shestakov mesh still contain some feature of their quadrilateral-equivalent. Table 2 summarizes the types and number of polygonal cells found in each of these grids. For example, there are six polygons with 11 sides in the Z-mesh of Fig. 7. The percentages of cells that are not triangular nor quadrangular for the random, Z-mesh, and Shestakov polygonal grids of Fig. 7 are 81%, 48%, and 73%, respectively. As with quadrilateral grids, the linearity of the true solution is exactly reproduced by the piece-wise linear discontinuous finite element solution on polygonal grids.

Grid of Fig. 6	# of convex cells / total # of cells
Random	54 / 256
Z-mesh	0 / 400
Shestakov	22 / 256
Shaskov	4 / 9

Table 1: Fraction of Concave Cells in Quadrilaterals Grids shown in Fig. 6

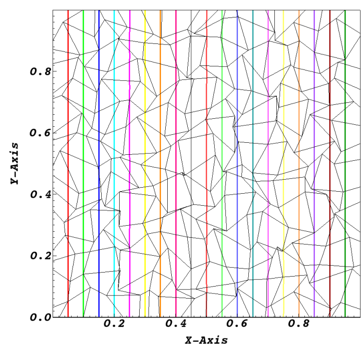

(a) Random quads, $\alpha = 0.66$

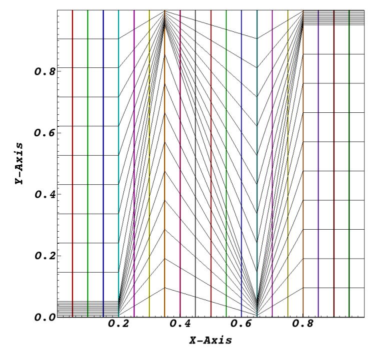

(b) Z-mesh, $s = 0.05$

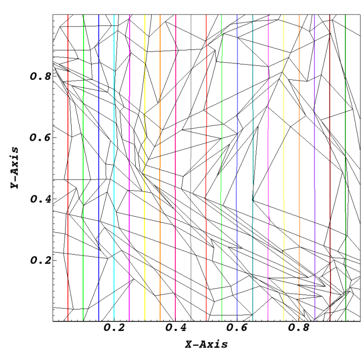

(c) Shestakov, $a = 0.15$

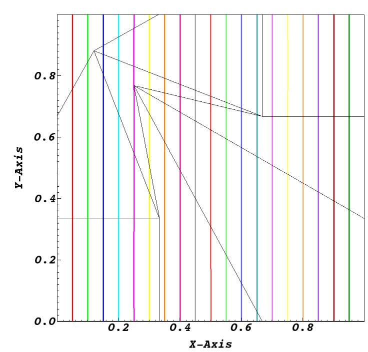

(d) Shaskov 3×3 mesh

Figure 6: Linear solutions on quadrilateral grids

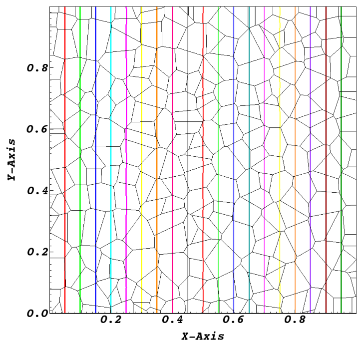

(a) Random polygons

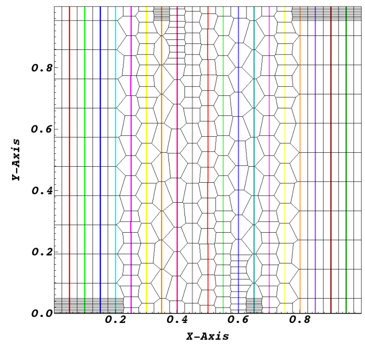

(b) Z-mesh

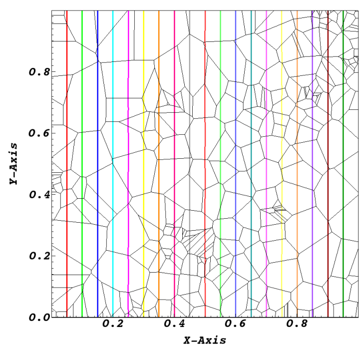

(c) Shestakov mesh

Figure 7: Linear solution on polygonal grids

Polygon type	Random	Z-mesh	Shestakov
Triangle	5	0	12
Quadrangle	43	228	65
Pentagon	73	72	83
Hexagon	67	81	50
Heptagon	41	48	36
Octagon	23	2	21
Nonagon	4	4	18
Decagon	0	0	2
Hendecagon	0	6	2

Table 2: Number and type of polygonal cells shown in Fig. 7

5.2. Convergence Rate Studies On Distorted Meshes

In this example, we compare the convergence rates of PWLD finite elements on several quadrilateral and polygonal meshes using the method of manufactured solutions [39]. Using the following exact solution,

$$E^{exa}(x,y) = \sin(\nu\pi x/L_x)\sin(\nu\pi y/L_y) \qquad \text{in } \mathcal{D} = [0,L_x]\times[0,L_y] \tag{20}$$

with zero-Dirichlet boundary conditions, $D = 1/6$, $\sigma_a = 1$, and ν, a frequency parameter, chosen to be 3 here, one can compute the corresponding volumetric source term $Q(x,y)$ for the diffusion equation. Then, by solving Eq. (1) on a sequence of grids with increasing resolution, one can determine the convergence rate of the error as a function of the number of unknowns. The L_2-norm of the error, ε_h, is defined in the usual manner:

$$\varepsilon_h^2 = \|E^{exa} - E_h\|_{\mathcal{D}}^2 = \int_{\mathcal{D}} \left[E^{exa}(x,y) - E_h(x,y)\right]^2 \, dxdy\,. \tag{21}$$

To compute with high accuracy the integral of a generic function f on an arbitrary polygonal partition $\mathbb{T}_h$ of $\mathcal{D}$, we sum the integration over each polygonal cell; the integration over each cell is split into its triangular sides (using two consecutive vertices and the cell center point); finally, the integration over each triangular side is performed by subdividing each triangle into three quadrangles for which a high-order standard 2D Gauss-Legendre quadrature is used. This can be summarized as follows:

$$\int_{\mathbb{T}_h} f = \sum_{K\in\mathbb{T}_h} \sum_{\text{sides of } K} \sum_{k=1}^{3}\sum_{q=1}^{N_q} w_q f_q\,. \tag{22}$$

Note that the same process (subdivision of K into sides that are further split into quadrangles) is also employed to compute accurately the contribution of the volumetric source to the system's right-hand side, $\int_K b_i Q$.

For uniform structured meshes, it is fairly straightforward to obtain the asymptotic convergence rate by plotting the error ε_h versus the mesh size h. Conversely, grid resolution is also related to the number of degrees of freedom, N_{dof} (unknowns) via

$$N_{dof} \propto h^{-\dim} \tag{23}$$

where dim is the dimensionality of the domain (here, dim $= 2$). Hence, a second-order convergence rate will translate into the error ε_h being linearly proportional to $1/N_{dof}$.

5.2.1. Distorted Quadrilateral Meshes

A convergence study is performed using four types of quadrilateral grids: uniform, Sinusoidal (with $\zeta = 0.15$), Shestakov mesh (with $a = 0.25$), and Z-mesh (with $s = 0.05$). For the Sinusoidal, Shestakov, and Z-mesh types, a series of embedded grids of increasing resolution is utilized (this is actually part of the standard construction process for these grids). For the random quadrilateral grids, we have simply generated one realization of a grid per refinement level. In Fig. 8, we show the 2×2, 8×8 , 32×32 , and 128×128 Shestakov grids used here. In Fig. 9, we show the 2×2, 8×8 , 32×32 , and 128×128 random grids used here.

The variation of the L_2 norm of the error as a function of the number of unknowns rate is graphed in Fig. 10 for quadrilateral grids. A slope of one is observed for all meshes except for Shestakov meshes. Thus, PWLD finite element discretization is second-order accurate for most quadrilateral meshes, even the ones with a significant amount of distortion, and exhibit reduced rates for highly distorted Shestakov meshes. To further analyze this observation, we provide the convergence rates for Shestakov and Z meshes in Fig. 11 as a function of the randomness parameter a (Shestakov meshes) and the skewness parameter s (Z meshes); recall that $0 \leq a\,, s \leq 0.5$ and that a value of 0.5 correspond to a structured rectangular grid and a value of close to 0 corresponds to a severely distorted/skewed grid. For $0.3 \leq a \leq 0.5$, PWLD retains second-order convergence on Shestakov grids but drastically looses such a rate for more distorted grids; this is not surprising and we are not aware of any spatial discretization technique able to preserve second-order convergence on such grids. For Z-meshes, second-order convergence is retained for all grids, even the highly skewed grid with $s = 0.05$ (shown in Fig. 12(e), for instance).

Finally, Fig. 12 presents some representative quadrilateral grids and the solution isolines (15 isolines, equally spaced by 0.125 in solution magnitude). The grids and isolines are not provided for the highest resolution data point found in Fig. 10 (but the third-to-last data point) so as to display the mesh effects (at higher grid resolutions, the grid imprints are no longer discernible).

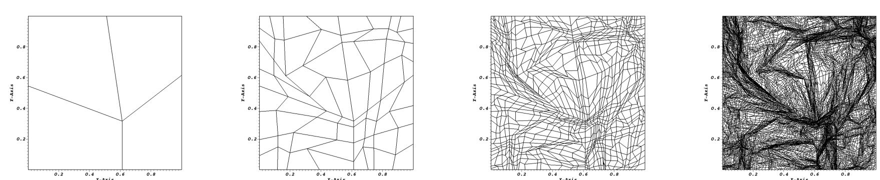

(a) 2×2 (b) 8×8 (c) 32×32 (d) 128×128

Figure 8: Quadrilateral Shestakov Grids ($a = 0.25$)

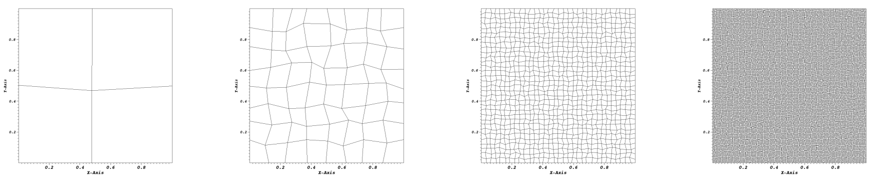

(a) 2×2 (b) 8×8 (c) 32×32 (d) 128×128

Figure 9: Quadrilateral Random Grids

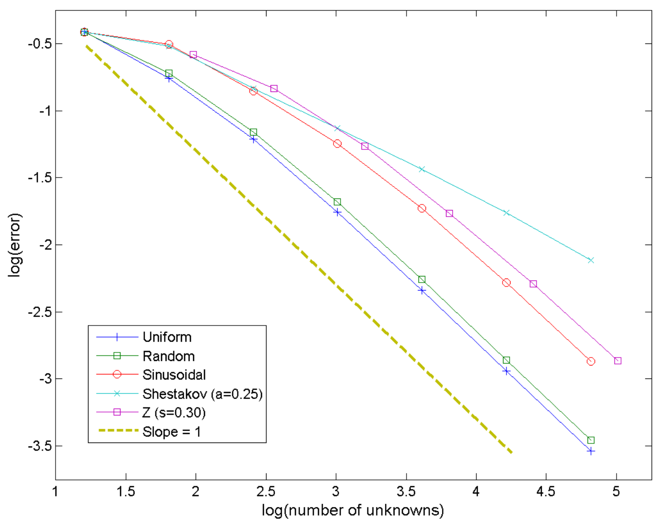

Figure 10: Convergence Study Using Quadrilateral Grids

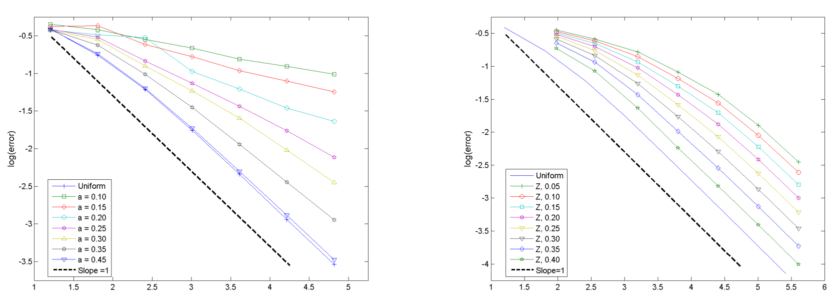

(a) Shestakov Meshes (b) Z Meshes

Figure 11: Convergence Rates for Shestakov and Z Quadrilateral Grids as a function of the randomness parameter a (Shestakov) and the skewness parameter s (Z)

5.2.2. Polygonal Meshes

We carry out the same study as in the previous Section but using polygonal grids this time. We employ the same terminology (random, sinusoidal, Shestakov, Z) to denote the polygonal meshes generated. However, recall that this denomination only describes the manner in which the vertices (used as input for the bounded Voronoi diagram) have been obtained. Fig. 13 shows the convergence rate study on polygonal grids. Second-order accuracy is observed for all grids, including the Shestakov grids generated with $a = 0.15$ and $a = 0.25$, and a Z-mesh obtained with a skewness coefficient of $s = 0.05$. Table 3 summarizes the types and number of polygonal cells used for the highest resolution point in Fig. 13. For instance, The percentages of cells that are not triangular nor quadrangular for the random, Sinusoidal, Z-mesh, and Shestakov polygonal grids are 87%, 94%, 58%, and 82%, respectively.

Finally, Fig. 14 presents some representative polygonal grids and the solution isolines (15 isolines, equally spaced by 0.125 in solution magnitude). The grids and isolines are not provided for the highest resolution data point of Fig. 13 so as to display more prominently some mesh effects (at increased resolutions, the grid imprints are no longer discernible).

Polygon type	Random	Sinusoidal	Z-mesh	Shestakov
Triangle	50	0	0	58
Quadrangle	489	231	2732	665
Pentagon	1080	588	696	1090
Hexagon	1299	2878	2585	1107
Heptagon	851	424	478	724
Octagon	351	104	40	363
Nonagon	79	0	10	154
Decagon	20	0	6	42
Hendecagon	5	0	4	14
Dodecagon	1	0	4	5
13 sides	0	0	2	2
14 sides	0	0	2	0
17 sides	0	0	0	1
22 sides	0	0	2	0

Table 3: Number and type of polygonal cells shown in Fig. 13

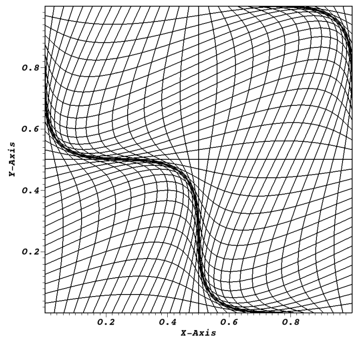

(a) 32×32 Sinusoidal ($\zeta = 0.15$), Mesh

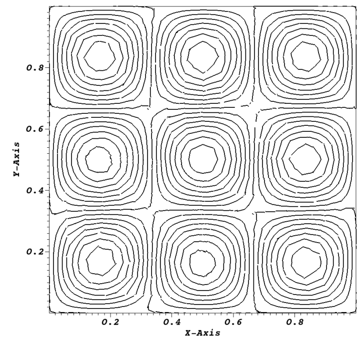

(b) 32×32 Sinusoidal ($\zeta = 0.15$), Isolines

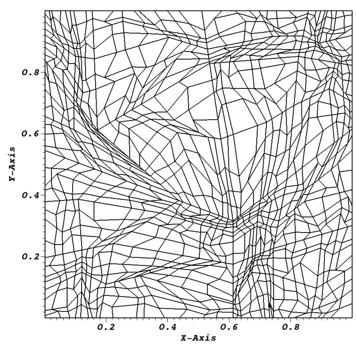

(c) 32×32 Shestakov ($a = 0.25$), Mesh

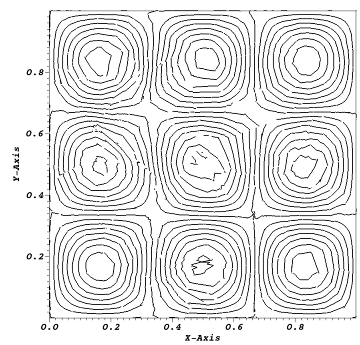

(d) 32×32 Shestakov ($a = 0.25$), Isolines

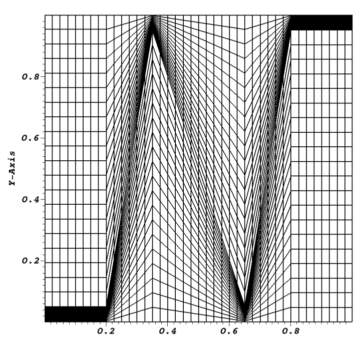

(e) 40×40 Z-mesh ($s = 0.05$), Mesh

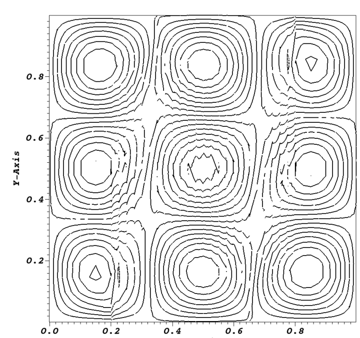

(f) 40×40 Z-mesh ($s = 0.05$), Isolines

Figure 12: Quadrilateral Grids and Solution isolines

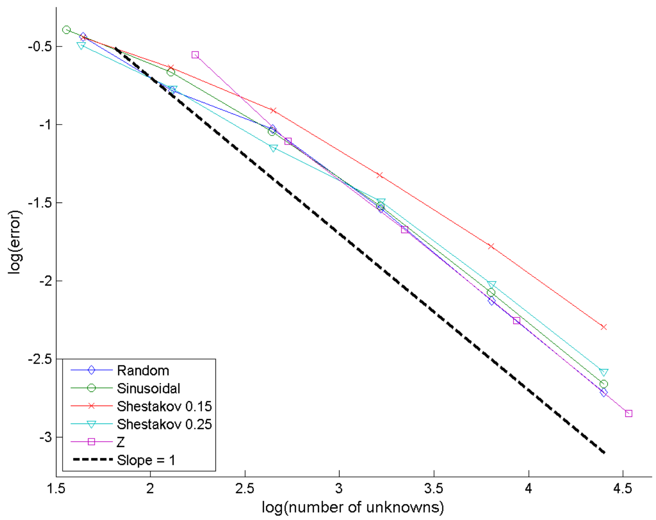

Figure 13: Convergence Study Using Polygonal Grids

5.3. Tensor Diffusion Tests Using Polygonal Grids

In this series of run, we replace the traditional diffusion coefficient with a full symmetry tensor,

$$D \longrightarrow \mathbb{D}\,. \tag{24}$$

In our numerical experiments, we use

$$\mathbb{D} = \begin{bmatrix} (x+1)^2 + y^2 & -xy \\ -xy & (x+1)^2 \end{bmatrix}, \tag{25}$$

as found in the test cases carried out for mimetic finite differences on polygonal grids in [3, 4]. The exact solution is again given by Eq. (20) with $\nu = 3$ on a unit square domain. With mimetic finite differences, the spatially varying coefficients and tensors are evaluated at the center of mass of the cells, whereas in our finite element discretization, they are evaluated at quadrature points. Specifically, the following changes were made to accommodate for the diffusion tensor: (1) the element stiffness matrix is now

$$\left(\mathbb{D}^{xx}\partial_x E + \mathbb{D}^{xy}\partial_y E\right)\partial_x b + \left(\mathbb{D}^{yx}\partial_x E + \mathbb{D}^{yy}\partial_y E\right)\partial_y b\,, \tag{26}$$

as it should be; (2) the integrand of the line integrals is modified as follows

$$D\partial_n E b = D\vec{\nabla} E \cdot \vec{n} b \longrightarrow \mathbb{D}\vec{\nabla} E \cdot \vec{n} b\,; \tag{27}$$

and, (3) the diffusion coefficient appearing in the penalty factor is replaced with the largest eigenvalue of the diffusion tensor at the edge's midpoint

$$\frac{C}{2}\left(\frac{D^+}{h_\perp^+} + \frac{D^-}{h_\perp^-}\right) \longrightarrow \frac{C}{2}\left(\frac{\|\mathbb{D}\|_2^+}{h_\perp^+} + \frac{\|\mathbb{D}\|_2^-}{h_\perp^-}\right), \tag{28}$$

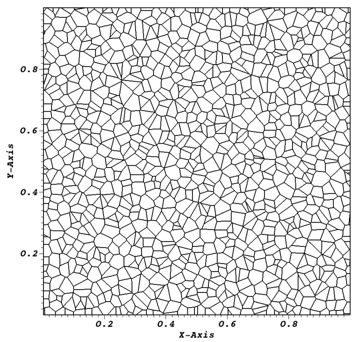

(a) Random Mesh (6374 N_{dof})

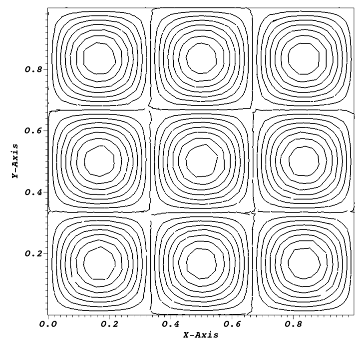

(b) Random Mesh Isolines

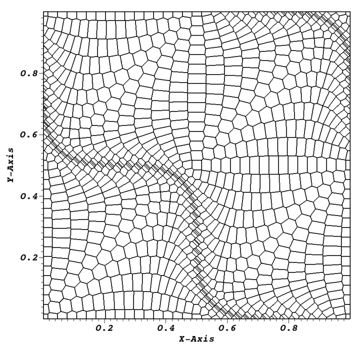

(c) Sinusoidal Mesh (6332 N_{dof})

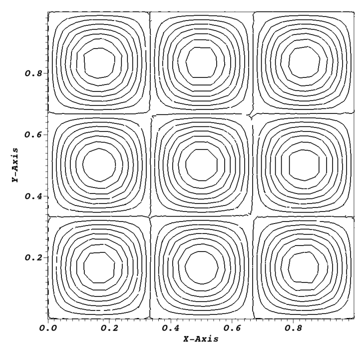

(d) Sinusoidal Mesh Isolines

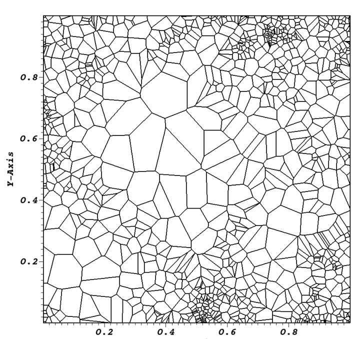

(e) Shestakov ($a = 0.10$) Mesh (6317 N_{dof})

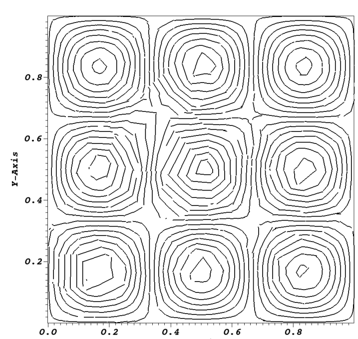

(f) Shestakov Mesh Isolines

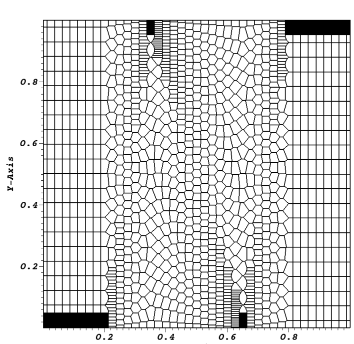

(g) Z-mesh ($s = 0.05$) (8644 N_{dof})

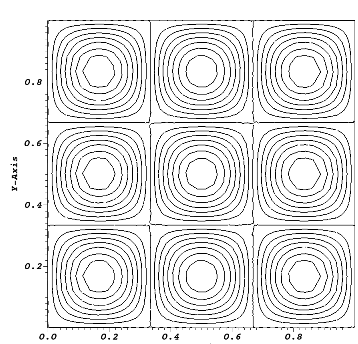

(h) Z-mesh Isolines

Figure 14: Polygonal Grids and Solution isolines

(we could have computed the largest eigenvalue of $\mathbb{D}$ at every quadrature point appearing in the edge integrals of the penalty term, but choosing the midpoint value avoids doing this while preserving second-order convergence).

The same polygonal grids as in Section 5.2.2 are used to study the convergence of the PWLD discretization for the tensor diffusion problem. Fig. 15 presents the convergence rates for these polygonal grids. Again, second-order accuracy is observed for all grids, including the Shestakov grids generated with $a = 0.15$, and a Z-mesh obtained with a skewness coefficient of $s = 0.05$.

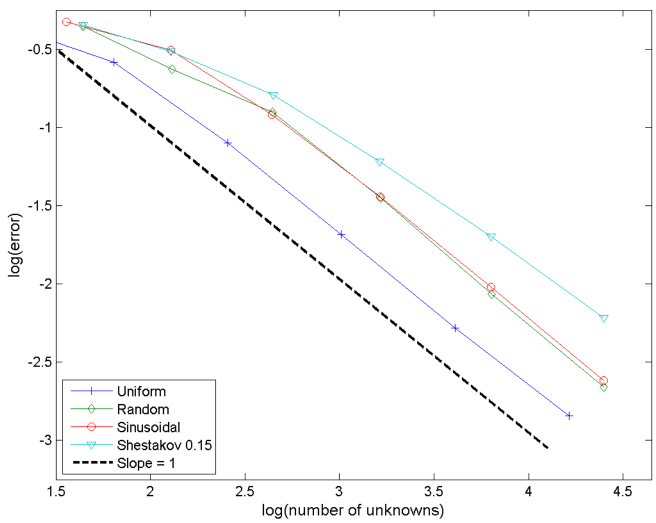

Figure 15: Rate of Convergence for the Tensor Diffusion Problem Using Polygonal Grids

5.4. Adaptive Mesh Refinement Using PWLD Finite Elements

In this Section, we use the PWLD discretization to seamlessly handle AMR grids and compare the rate of convergence rate of AMR grids with the ones of uniformly refined grids. In the AMR process, the cells whose error is within 20% of the maximum detected error are flagged for refinement, that is, a value of $\theta = 0.8$ is employed in Eq. (16). To compare the numerical errors and obtain the rate of convergence, we employ again the method of manufactured solutions. This time, a rapidly spatially varying function is chosen as the exact solution:

$$E^{exa}(x,y) = 100\frac{xy(L_x-x)(L_y-y)}{(L_xL_y)^2}\exp\Big(-\frac{(x-x_0)^2+(y-y_0)^2}{\varsigma}\Big) \quad \text{in } \mathcal{D} = [0,L_x]\times[0,L_y]\,. \tag{29}$$

We have chosen the location of the peak to be $x_0 = \frac{6}{10}L_x$, $y_0 = \frac{7}{10}L_y$, with $\varsigma = L_xL_y/100$. The diffusion coefficient and absorption cross section are $D = 1/6$

and $\sigma_a = 1$. This exact solution satisfies zero-Dirichlet boundary conditions. One then can compute the corresponding volumetric source term $Q(x, y)$ used to generate the right-hand of the discrete linear system. We solve the radiation diffusion equation on a sequence of grids with increasing resolution. The coarsest grid level uses simply a 2×2 grid with quadrangles. This initial grid is either uniformly refined or locally adapted using the refinement criteria set forth in Section 4. The L_2-norm of the error (difference between the exact and the computed numerical solutions) is plotted in Fig. 16. As expected, both refinement strategies lead to a convergence rate of one measured against the number of unknowns, demonstrating the second-order accuracy of PWLD discretization on both grid types. We note that when using an AMR strategy the solution is obtained with roughly a savings of a factor of 5 to 6 in terms of the number of unknowns. The numerical solution obtained with AMR is graphed on Fig. 17. Fig. 18 shows the AMR grids at cycles 5, 10, 15, and 20. The location of peak in the exact solution is locally refined as the number of adaptivity cycles increases. Fig. 18(d) presents a zoom on the AMR grid of cycle 15 where one can note the presences of several (degenerated) octogonal cells surrounded by once-more refined neighbors on all of their sides. Since these cells possess eight unknowns with the PWLD discretization, as opposed to only four with a standard bilinear discontinuous discretization, the 3-irregular rule of Bank does not need to be applied. Table 4 provides the types and number of polygonal cells used in the last AMR grid.

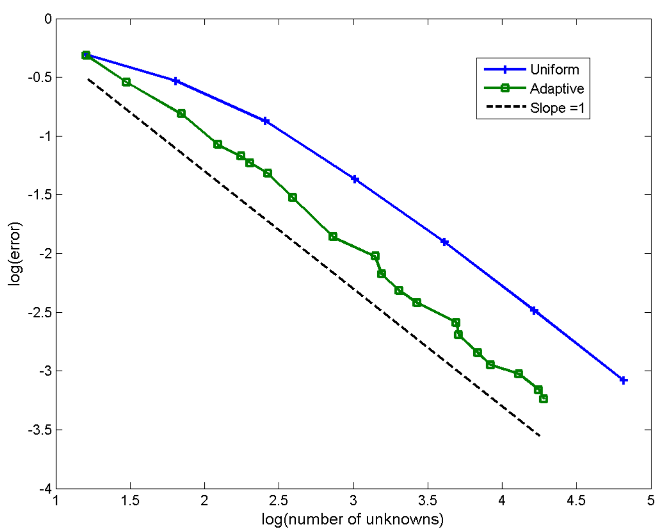

Figure 16: Rate of Convergence Using Uniform and Locally Adapted Grids

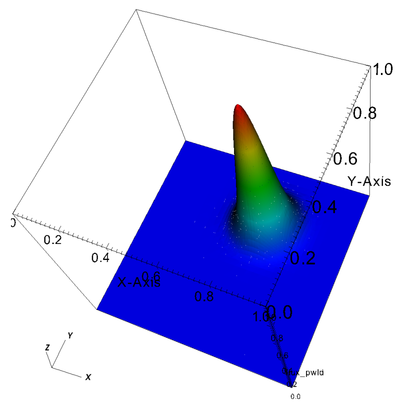

Figure 17: Numerical solution at the last adaptivity cycle

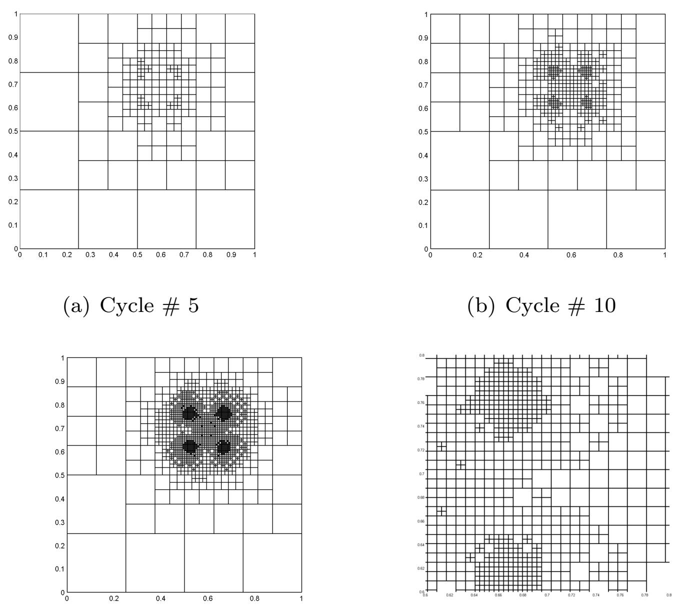

(a) Cycle # 5

(b) Cycle # 10

(c) Cycle # 15

(d) Zoom (Cycle # 15)

Figure 18: AMR Grids at various adaptivity cycles

Quadrangle	8297
Pentagon	446
Hexagon	227
Heptagon	56
Octagon	98

Table 4: Number and type of polygonal cells at adaptivity cycle # 20

6. Conclusions

A piece-wise linear discontinuous (PWLD) finite element discretization has been applied to the radiation diffusion equation on arbitrary polygonal grids. The Symmetric Interior Penalty stabilization technique has been employed and extended to polygonal cells. The resulting linear system is SPD and can be effectively solved using PCG. Second-order convergence has been numerically verified on highly distorted grids. Polygonal grids have been generated from bounded Voronoi diagrams created using vertex locations from severely distorted quadrilateral grids; many meshes contain polygons with a high number of vertices (e.g., > 6).

One of the attractive features of a PWL discretization lies in its handling of locally refined grids. Cells adjacent to more refined cells do not possess hanging nodes on the common edges with the refined cells but rather the nature of the coarse cell is changed to that of a polygon with additional sides. We have fully embedded this characteristic of PWL finite elements within an automated adaptive mesh refinement process and verified that second-order convergence was retained while reducing the number of unknowns for the same level of accuracy when compared with uniformly refined quadrilateral grids.

This paper shows that the radiation diffusion equation can be effectively discretized on arbitrary polygonal meshes using a piece-wise linear discontinuous finite element approximation. This will allow us to use proven DFEM-based DSA preconditioners [23] to tackle radiation transport problems on polygonal grids in the future and will be the topic of subsequent publications.

Acknowledgments

The author is grateful to Dr. Alex Shestakov (LLNL) for providing Reference [36] and for suggesting studying smooth meshes (Sinusoidal grids) as well. We would also like to acknowledge Dr. Michael Hall (LANL) for retrieving a Fortran77 copy of the “Shestakov” program.

References

[1] Wachspress. *A Rationale Finite Element Basis*. New York : Academic Press, 1975.

[2] Todd S. Palmer. Discretizing the diffusion equation on unstructured polygonal meshes in two dimensions. *Annals of Nuclear Energy*, 28(18):1851 – 1880, 2001.

[3] Y. Kuznetsov, K. Lipnikov, and M. Shashkov. The mimetic finite difference method on polygonal meshes for diffusion-type problems. *Computational Geosciences*, 8:301–324, 2004.

[4] Franco Brezzi, Konstantin Lipnikov, and Valeria Simoncini. A Family of Mimetic Finite Difference Methods on Polygonal and Polyhedral Meshes. *Math. Models Methods Appl. Sci.*, 15(10):1533–1551, 2005.

[5] Konstantin Lipnikov, Mikhail Shashkov, and Daniil Svyatskiy. The mimetic finite difference discretization of diffusion problem on unstructured polyhedral meshes. *Journal of Computational Physics*, 211(2):473 – 491, 2006.

[6] Teresa S. Bailey. *The piecewise linear discontinuous finite element method applied to the RZ and XYZ transport equations*. PhD thesis, Texas A&M University, 2008.

[7] Teresa S. Bailey, Marvin L. Adams, Brian Yang, and Michael R. Zika. A piecewise linear finite elements discretization of the diffusion equation for arbitrary polyhedral grids. *Journal of Computational Physics*, 227:3738–3757, 2008.

[8] K. Lipnikov and M. Shashkov. A framework for developing a mimetic tensor artificial viscosity for lagrangian hydrocodes on arbitrary polygonal meshes. *Journal of Computational Physics*, 229(20):7911 – 7941, 2010.

[9] T. S. Palmer. Unstructured polyhedral mesh thermal radiation diffusion. *American Nuclear Society Winter Meeting*, Nov. 12-16 2000. Washington, DC.

[10] J. Hyman, J. Morel, M. Shashkov, and S. Steinberg. Mimetic finite difference methods for diffusion equations. *Computational Geosciences*, 6:333–352, 2002.

[11] J.E. Morel, Randy M. Roberts, and Mikhail J. Shashkov. A local support-operators diffusion discretization scheme for quadrilateral r-z meshes. *Journal of Computational Physics*, 144(1):17 – 51, 1998.

[12] J.E. Morel, Michael L. Hall, and Mikhail J. Shashkov. A Local Support-Operators Diffusion Discretization Scheme for Hexahedral Meshes. *Journal of Computational Physics*, 170(1):338 – 372, 2001.

[13] D. N. Arnold. An interior penalty finite element method with discontinuous elements. *SIAM J. Numer. Anal.*, 19:742–760, 1982.

[14] Douglas N. Arnold, Franco Brezzi, Bernardo Cockburn, and L. Donatella Marini. Unified analysis of discontinuous galerkin methods for elliptic problems. *SIAM J. Numer. Anal.*, 39(5):1749–1779, 2002.

[15] G. Kanschat. *Discontinuous Galerkin Methods for Viscous Incompressible Flow*. Advances in Numerical Mathematics. Teubner Research, Wiesbaden, Germany, 2007.

[16] Marvin L. Adams and Edward W. Larsen. Fast iterative methods for discrete-ordinates particle transport calculations. *Progress in Nuclear Energy*, 40:3–159, 2002.

[17] James S. Warsa, Todd A. Wareing, and Jim E. Morel. Krylov iterative methods and the degraded effectiveness of diffusion synthetic acceleration for multidimensional S_N calculations in problems with material discontinuities. *Nucl. Sci. Eng.*, 147:218–248, 2004.

[18] Todd A. Wareing, John M. McGhee, Jim E. Morel, and Shawn D. Pautz. Discontinuous finite element S_N methods on three-dimensional unstructured grids. *Nucl. Sci. Eng.*, 138:256–268, 2001.

[19] James S. Warsa. A Continuous Finite Element-Based, Discontinuous Finite Element Method for Sn Transport. *Nuclear Science and Engineering*, 160:385–400, 2008.

[20] Yaqi Wang and Jean C. Ragusa. On the convergence of dgfem applied to the discrete ordinates transport equation for structured and unstructured triangular meshes. *Nuclear Science and Engineering*, 163:56–72, 2009.

[21] Teresa S. Bailey, James S. Warsa, Jae H. Chang, and Marvin L. Adams. A Piecewise Bi-Linear Finie Element Spatial Discretization of the S_n Transport Equation. *International Conference on Mathematics and Compuational Methods Applied to Nuclear Science and Engineering*, May 8-12 2011. Rio de Janeiro, Brazil.

[22] Yaqi Wang and Jean C. Ragusa. Standard and goal-oriented adaptive mesh refinement applied to radiation transport on 2d unstructured triangular meshes. *Journal of Computational Physics*, 230:763–788, 2011.

[23] Yaqi Wang and Jean C. Ragusa. Diffusion synthetic acceleration for high-order discontinuous finite element S_N transport schemes and application to locally refined unstructured meshes. *Nuclear Science and Engineering*, 166:145–166, 2010.

[24] R. V. Garimella. Mstk: A flexible infrastructure library for developing mesh-based applications. In *Proceedings of the 13th International Meshing Roundtable, Williamsburg, VA.*, 2004.

[25] Cgal, Computational Geometry Algorithms Library. http://www.cgal.org.

[26] Geert-Jan Giezeman and Wieger Wesselink. 2D polygons. In *CGAL User and Reference Manual*. CGAL Editorial Board, 4.2 edition, 2013. http://www.cgal.org/Manual/4.2/doc_html/cgal_manual/packages.html#Pkg:Polygon2.

[27] J.L. Lions. Problemes aux limites non homogenes a donnees irregulieres. In JacquesLouis Lions, editor, *Numerical Analysis of Partial Differential Equations*, volume 44 of *C.I.M.E. Summer Schools*, pages 283–292. Springer Berlin Heidelberg, 2011.

[28] J. Nitsche. Über ein Variationsprinzip zur Lösung von Dirichlet-Problemen bei der Verwendung von Teilräumen, die keinen Randbedingungen unterworfen sind. *Abh. Math. Univ. Hamburg*, 36:9–15, 1971.

[29] Bruno Turcksin. *Acceleration Techniques For Discrete-Ordinates Transport Methods With Highly Forward-Peaked Scattering*. PhD thesis, Texas A&M University, 2012.

[30] M. Ainsworth and J. T. Oden. *A posteriori Error Estimation in Finite Element Analysis*. John Wiley & Sons, New York, NY, 2000.

[31] Tobias Leicht and Ralf Hartmann. Anisotropic mesh refinement for discontinuous galerkin methods in two-dimensional aerodynamic flow simulations. *International Journal for Numerical Methods in Fluids*, 56(11):2111–2138, 2008.

[32] R.E. Bank. An efficient implementation of local mesh refinement algorithms. In J.E. Flaherty I. Babuka, J. Chandra, editor, *Adaptive Computational Methods for Partial Differential Equations*, pages 74–81. SIAM, Philadelphia, PA, 1983.

[33] J.E Morel, J.E Dendy Jr., Michael L Hall, and Stephen W White. A cell-centered lagrangian-mesh diffusion differencing scheme. *Journal of Computational Physics*, 103(2):286 – 299, 1992.

[34] David S Kershaw. Differencing of the diffusion equation in lagrangian hydrodynamic codes. *Journal of Computational Physics*, 39(2):375 – 395, 1981.

[35] A.I Shestakov, J.A Harte, and D.S Kershaw. Solution of the diffusion equation by finite elements in lagrangian hydrodynamic codes. *Journal of Computational Physics*, 76(2):385 – 413, 1988.

[36] A. Shestakov, D. Kershaw, and G. Zimmerman. Test problems in radiative transfer calculations. *Nuclear Science and Engineering*, 105:88–104, 1990.

[37] Yvan Notay. An Aggregation-Based Algebraic Multigrid Met. *Electronic Transactions on Numerical Analysis*, 37:123–146, 2010.

[38] Mikhail Shashkov and Stanly Steinberg. Solving diffusion equations with rough coefficients in rough grids. *Journal of Computational Physics*, 129(2):383 – 405, 1996.

[39] Patrick J. Roache. *Fundamentals of Verification and Validation*. Hermosa Publishers, September, 2009.

Compressed File of Latex files

Click here to download Compressed File of Latex files: submission.zip